Boosting solar photothermal synergy for efficient overall water splitting based on Mg, Al codoped and Rh/Cr$_2$O$_3$/CoOOH coloaded SrTiO$_3$

Xuan Zhu, Yan Liu, Menglin Wang, Li Zhang, Qiaoli Li, Entao Zhang, Hongfen Mo, Yuan Gao, Chenyu Xu [*], Yanwei Zhang [*]

State Key Laboratory of Clean Energy Utilization, Zhejiang University, Hangzhou 310027, China

ABSTRACT

The synergistic coupling of light and heat in solar energy has attracted increasing research attention. In this work, both codoping and coloading were applied to SrTiO$_3$-based catalysts to improve their solar photo and thermal conversion, respectively, and maximum productivities of 51.55 and 25.59 mmol·g^{-1}·h^{-1} were achieved for H$_2$ and O$_2$ in photothermal synergistic water splitting. The yield of H$_2$ was nearly double that achieved via pure photocatalysis. In addition to many experiments and characterizations, DFT calculations were also performed to clarify the photothermal synergy. It was found that both the light absorbance and mobility of photoinduced carriers could be promoted by solar thermal effects in the material. Meanwhile, the energy barriers of the key steps were reduced with increasing temperature in the hydrogen production driven by solar photo effects. This work offers new ideas for designing catalysts for solar hydrogen production with photothermal synergistic strategies.

1. Introduction

With the rapid development of society, environmental issues have become a key concern that cannot be ignored; in particular, the massive use of fossil energy has caused environmental pollution and greenhouse gas emissions, and there is an urgent need to find ways to replace fossil energy to reduce environmental pollution [1–7]. As an inexhaustible source of clean energy, solar energy is attracting increasing attention due to its sustainability and variety of conversion and utilization methods [8–11]. Photothermal catalytic water splitting is an effective means of solar energy utilization that can directly convert the Earth's abundant water into hydrogen and oxygen without producing any polluting substances in the whole process [12–14]. In addition, hydrogen energy is a clean and efficient renewable energy source with high application value and can promote clean energy transformation [15–19]. Therefore, the production of hydrogen using solar energy to achieve overall water splitting is an alternative to the use of fossil energy [20–22].

During the conversion of solar energy as the sole energy source into hydrogen energy, the photo effect and the thermal effect occur simultaneously [23]. The main spectral region that can be utilized for photocatalysis technology is the ultraviolet region due to the band gap limitation of semiconductor materials, which accounts for only approximately 5 % of the total solar spectrum (290 nm-400 nm) [24]. The proportion of infrared light in the solar spectrum is more than 50 % (>760 nm), and this part of the energy makes it difficult to excite the semiconductor to produce carriers for the water decomposition reaction [25], which is then absorbed by the semiconductor and converted into heat, resulting in a change in temperature during the reaction [26]. However, in most photocatalytic reactions, a water cooling circuit is usually added to maintain the ambient temperature, which often ignores the influence of thermal effects [27–29]. In many catalytic reactions, temperature serves as a positive factor in promoting catalytic activity [30–32]. If photothermal synergy can be achieved in water splitting reactions, it not only increases the photocatalytic activity through thermal effects but also effectively utilizes the abundant infrared light from the solar spectrum, thereby improving the efficiency of solar energy utilization. Therefore, in the context of solar-driven photothermal catalytic water splitting, investigating the mechanism of the synergism between the photoeffect and thermal effect is particularly crucial for increasing the activity of the water splitting reaction.

SrTiO$_3$, which is a typical photocatalyst with a perovskite structure, is a wide bandgap semiconductor with a suitable water-splitting energy band position and relatively stable physicochemical properties and has

---

* Corresponding authors.
  E-mail addresses: mrxcy@zju.edu.cn (C. Xu), zhangyw@zju.edu.cn (Y. Zhang).

been increasingly studied [33–36]. Research on SrTiO$_3$ includes doping with transition metal ions and rare earth metals, designing heterogeneous structures, and constructing z-type photocatalytic systems for efficient water splitting [37,38]. In recent years, some researchers have focused on low-valent cation doping strategies to enhance the water splitting activity of SrTiO$_3$ [39]. Domen [40] used low-valent cations such as Na$^+$ and Al^{3+} to dope SrTiO$_3$ and found that low-valent cation doping can introduce oxygen vacancies and reduce the number of defects such as Ti^{3+} to improve photocatalytic water splitting activity. Meanwhile, the treatment with SrCl$_2$ can improve the crystallinity of SrTiO$_3$ and promote the doping of Al by flux method, which can further improve the H$_2$ yield [39]. Furthermore, it was found that the introduction of Mg^{2+} doping could also result in a greater photocatalytic hydrolysis ability [41], but the specific mechanism underlying this effect remains unexplained; Hence, it is essential to investigate Mg^{2+} doping to enhance the photocatalytic water splitting activity to better understanding of the effect of doping different low-valent cations on the performance of photocatalysts. In overall photocatalytic water splitting, Rh/Cr$_2$O$_3$ and CoOOH have been extensively studied as a hydrogen evolution catalyst and an oxygen evolution catalyst [42], respectively. However, there is a paucity of reports focusing on their favorable photothermal effects. Due to the wide band gap of SrTiO$_3$, the main light absorption region is the ultraviolet part. Previous studies have often focused on modifying the UV absorption properties of SrTiO$_3$ or broadening it to the near-visible part by doping, etc., but the thermal effect on water splitting caused by nearly 50 % of the infrared light in the solar spectrum has often been neglected.

In this study, a novel photothermal catalyst, consisting of a 1 % Mg-Al codoped SrTiO$_3$ sample loaded with Rh/Cr$_2$O$_3$/CoOOH was designed for the photothermal catalytic water splitting reaction. The introduction of Al^{3+} effectively reduced the Ti^{3+} content and increased the concentration of oxygen vacancies. At the same time, the oxygen vacancy content was further increased after the introduction of Mg^{2+}, which enhanced the adsorption of water molecules and reduced the radiative recombination of photogenerated carriers. These factors significantly enhanced the photoeffect of SrTiO$_3$. The loading of the Rh/Cr$_2$O$_3$ and CoOOH cocatalysts both improved the separation of photogenerated electron-hole pairs and induced a significant photothermal effect, with an increase in the surface temperature of 51 °C compared to that of the sample without cocatalysts. In comparison to that of pure photocatalytic reactions, the yield of H$_2$ under conditions of photothermal synergy was almost two times higher. A comprehensive temperature-dependent characterization was carried out to elucidate the impact of thermal effects on the performance of the catalyst. It was found that with increasing temperature due to thermal effects, the catalyst exhibited a significant increase in photocurrent, a decrease in impedance, a narrowing of the bandgap, enhanced spectral absorption, and a reduction in carrier recombination. Furthermore, DFT calculations confirmed that increasing the temperature lowered the energy barrier of key reaction steps and promoted the desorption of products. Therefore, these results contributed to the remarkable improvement in water splitting productivity in the photothermal synergistic reaction. In this study, it was found that synergizing the photoeffect with the thermal effect can effectively enhance the yield of water splitting, which can utilize the thermal effect of infrared light to promote solar energy conversion. The synergistic mechanism of the photoeffect and thermal effect based on Mg, Al codoped SrTiO$_3$ to enhance the photothermal catalytic water splitting performance was also revealed.

2. Experimental section

2.1. Chemicals and materials

The nanosized strontium titanate (SrTiO$_3$, 99.5 % metal basis, < 100 nm) was purchased from Meryer Biochemical Technology Co., Ltd.). (Shanghai). Strontium chloride (SrCl$_2$, 99.0 % purity) was purchased

from Leyan (Shanghai Haohong Scientific Co., Ltd.). Nanosized magnesium oxide (MgO, 99.9 % metal basis) and potassium chromate (K$_2$CrO$_4$, 99.5 % metal basis) were purchased from Macklin (Biochemical Co., Ltd). (Shanghai). Rhodium chloride hydrate (RhCl$_3$·3H$_2$O, 38.5–42.5 % Rh basis) was purchased from Aladdin (Biochemical Technology Co., Ltd.). (Shanghai). Cobalt(II)nitrate hexahydrate (Co (NO$_3$)$_2$·6H$_2$O) was purchased from Sinopharm Chemical Reagent Co., Ltd.

2.2. Synthesis of catalysts

The Mg, Al codoped SrTiO$_3$ samples in this work were prepared using the flux treatment method [39]. Specifically, SrTiO$_3$, MgO, and SrCl$_2$ were mixed by grinding in an agate crucible for a certain time at molar ratios of 1:0:10, 1:0.005:10, 1:0.01:10, 1:0.02:10, and 1:0.03:10. Then, each mixture was transferred to an alumina crucible and calcined in a muffle furnace at 1423 K for 10 h in the air. Following that, the sample was washed with water to remove excess SrCl$_2$ until no Cl$^-$ was observed in the filtrate. Finally, these samples were dried in an oven overnight before the next tests. The obtained 0 to 3 % Mg-doped Al-SrTiO$_3$ (Al was supplied by the Al$_2$O$_3$ crucible) samples were denoted 0 % Mg-AlSTO, 0.5 % Mg-AlSTO, 1 % Mg-AlSTO, 2 % Mg-AlSTO, and 3 % Mg-AlSTO. For further comparison, a pure SrTiO$_3$ (STO) sample was prepared without any pretreatment.

2.3. Loading of cocatalysts

An in situ photodeposition method was used for cocatalyst loading. The steps were as follows: 100 mg of the sample was dispersed in a certain amount of water for ultrasonic pretreatment, followed by continuous magnetic stirring in a beaker. Afterward, 0.1 wt% Rh (RhCl$_3$·3H$_2$O), 0.05 wt% Cr (K$_2$CrO$_4$), and 0.05 wt% Co (Co (NO$_3$)$_2$·6H$_2$O) were added sequentially, and the mixture was continuously irradiated using a xenon lamp. Finally, the suspension was centrifuged and dried to obtain the sample.

2.4. Characterizations

X-ray diffraction (XRD) patterns were obtained on a Rigaku Smart-Lab SE (Japan) equipped with a Cu Kα radiation source at 40 kV and 40 mA. Field emission scanning electron microscopy (SEM) was performed by means of a Hitachi SU8010 with an Oxford X-max80 X-ray spectrometer. High-resolution transmission electron microscopy (HR-TEM, FEI Talos F200S) combined with energy dispersive X-ray spectroscopy (EDX) was used to determine the sample microstructure and elemental distribution. X-ray photoelectron spectroscopy (XPS) was conducted by means of a Thermo Scientific K-Alpha with an Al Kα radiation source (hv = 1486.6 eV). The C 1 s peak, at a binding energy of 284.8 eV, served as a reference for the charge calibration of the data for all samples. The specific proportion of metal elements in the catalysts was determined by inductively coupled plasma–optical emission spectrometry (ICP–OES/ MS, Thermo Fisher iCAP PRO(OES), PerkinElmer NexION 2000(MS)). The specific test steps are as follows: before testing, the sample to be measured must be treated in an ionic solution. The sample was weighed and transferred to an 80 mL ablation beaker of PTFE material and wetted with a small amount of deionized water. Then 5 mL of concentrated nitric acid, 3 mL of hydrofluoric acid, and 2.0 mL of phosphoric acid were added and heated to 220 °C for elimination. When 1 mL of solution remained, 10 mL of aqua regia was added to continue digestion for a while and then transferred to a volumetric flask for volume determination after cooling. In the next step, 5 different concentrations of 100 mL standard solutions of the ions to be tested were prepared as a reference, and the signal value of the standard solution of each element was tested and fitted to obtain the concentration-signal curve, which was used to calibrate the actual elemental content of the samples to be tested. A UV–vis spectrophotometer (200–1400 nm, Shimadzu UV-2600,

and Shimadzu UV-3600 iplus) was used to conduct UV–visible diffuse reflectance spectroscopy (UV–vis DRS). The recombination of photo-generated carriers in the catalysts was determined from the photo-luminescence (PL) emission spectrum (Edinburgh FLS980) with a 365 nm excitation lamp, and all catalysts were tested with 20 mg powder samples. Electron paramagnetic resonance (EPR) was conducted on a Bruker EMXplus at a temperature of 120 K. The BET test was conducted on Micromeritics ASAP 2460.

2.5. Electrochemical measurements

Five milligrams of catalyst was mixed with 1 mL of anhydrous ethanol and a few drops of Nafion solution. After ultrasonic treatment, the appropriate amount of the mixture was uniformly dropped onto indium-tin oxide (ITO) conductive glass. All electrochemical charac-terizations were carried out using the IVIUMSTAT electrochemical interface. In a typical three-electrode cell, the platinum plate electrode served as the counter electrode, while the Ag/AgCl/saturated KCl elec-trode served as the reference electrode, and ITO with the catalyst was used as the working electrode. A 0.5 M Na_2SO_4 solution was applied as an electrolyte. A 365 nm LED (Fig. S4b) was employed as the light source. For the photocurrent test, after connecting the circuit, the applied potential was set to 0.5 V vs. Ag/AgCl. After the current baseline was stabilized, a monochromatic light source as the excitation light source, maintaining the switching frequency of the light source for 30 s each time and recording the change in the current signal. In the test of electrochemical impedance spectra, the frequency was perturbed from 0.1 MHz to 0.1 Hz, and five frequency measurement points were taken within each order of magnitude. In the Mott-Schottky curve test, the voltage sweep mode was turned on while the system was in equilibrium and the impedance value was calculated at a specific frequency. The voltage range was set to −0.7 to 0.3 V vs. Ag/AgCl and the applied frequency was 1000 Hz. According to the Mott-Schottky formula:

$$C^{-2} = \frac{2}{\varepsilon_r \varepsilon_0 eN}\left(E - E_{fb} - \frac{kT}{e}\right)$$

The Mott-Schottky curve of the working electrode can be obtained by plotting C^{-2} against voltage E.

2.6. Photothermal catalytic water splitting measurements

The water splitting reaction was realized in a closed gas circulation system. The gas products were detected by a gas chromatography (GC) system with a thermal conductivity detector (Agilent 7820 A, Ar serving as the carrier gas). Typically, 10 mg of catalyst was dispersed in water for sonication, and then the mixture was placed on a quartz fiber filter membrane to form a 3 cm diameter catalytic layer. The catalytic membrane was placed in the quartz reactor, and a certain amount of water was added to hold the catalytic membrane at the gas–liquid interface (Fig. S1a).

The effect of different temperatures on catalytic activity was explored using another reaction mode. Specifically, Fig. S1b displays schematics of the catalyst and water supply structures. The cotton in the middle was used as a water transport material, and the catalytic mem-brane was placed on the cotton to carry out the photothermal catalytic water splitting reaction. A piece of perforated polyethylene foam was used as a support material to hold the cotton in the reaction vessel. The chemical reaction was induced by a 365 nm LED with oblique incidence, while a Xe lamp with a UV–VIS cutoff filter (>800 nm) was used to determine the effect of temperature on the chemical reaction. Each set of tests was performed with the LED irradiated for 1 h, then the xenon lamp was turned on simultaneously to continue the test for 1 h, and finally the xenon lamp alone was used for 1 h to eliminate the catalytic effect of the xenon lamp itself on the catalyst.

2.7. Computational methods

First-principles calculations were performed using the CP2K Quick-step package [43]. The calculations were performed within the DFT formalism using the PBE-GGA exchange correlation functional [44]. The empirical correction in the DFT-D3 method with Becke-Jonson damping was used for long-range dispersion corrections [45]. Norm-conserving GTH pseudopotentials were used to describe the core electrons [46]. Gaussian functions consisting of a double-ζ valence polarized (DZVP) basis set were employed to optimize the structures. To further reduce the impact of basis set superposition errors (BSSEs), triple-ζ valence polar-ized (TZVP) basis sets were employed to calculate the single-point en-ergy. The cutoff energy of an auxiliary basis set of plane waves was 500 Ry. During the calculations, all of the atomic positions were fully relaxed until the force was smaller than 1×10^{-4} a.u./bohr. The convergence threshold for the self-consistent-field iteration was set to 1×10^{-7} a.u. The convergence accuracy of energy was set to 1×10^{-14} a.u.

The Rh metal loaded on the 100 crystalline surface in STO was the main highly reactive site, and thus, the complete water splitting reaction pathway was established at that site. The cubic $SrTiO_3$ (1 0 0) surface was modeled as a three-layer-thick slab with a 3×3 surface supercell ($Sr_{27}Ti_{27}O_{91}$). Then, the $SrTiO_3$ (1 0 0) surface was modified with Mg, Al, Vo (oxygen vacancy) and Rh_6. k-space sampling was restricted to the Γ point. To avoid the interaction between adjacent slabs, a vacuum layer thickness of 15 Å was chosen along the surface normal direction. We explored the hydrogenation reaction by calculating the Gibbs free en-ergy (ΔG) of the key intermediate under the specific photothermal conditions (p = 1 bar, T = 303.15 K, 323.15 K, 343.15 K, 363.15 K, 383.15 K, 383.15 K, 403.15 K). The Gibbs free energy of the in-termediates was calculated as ΔG = ΔE + ΔZPE – TΔS. ΔE is the reaction energy obtained from DFT. ΔZPE and ΔS are the differences in the zero-point energies and the change in entropy, respectively, which can be gained from the vibration energy of the intermediates using Shermo [47].

## 3. Results and discussion

3.1. Structure characterization

The XRD patterns of the prepared catalysts are shown in Fig. 1a (JCPDS no. 74–1296). The patterns of all the samples exhibited distinct diffraction peaks of $SrTiO_3$ in the range of 5°-90°, corresponding to the (1 0 0), (1 1 0), (1 1 1), (2 0 0), (0 1 2), (2 1 1), (2 2 0), (2 2 1), (0 1 3), (3 1 1), and (2 2 2) crystal planes, indicating that the codoping of Mg and Al did not significantly change the perovskite-type structures of $SrTiO_3$. The XRD spectrum of 1 % Mg-AlSTO loaded with cocatalysts is shown in Fig. S5. Due to the low loading of the cocatalyst, the figure does not show an obvious peak for RhCrCo, and the crystal of the catalyst did not change significantly after the loading of the cocatalyst. The lattice pa-rameters of these $SrTiO_3$-based modified materials are shown in Table S1 and Fig. 1b. First, the lattice constants of $SrTiO_3$ treated in alumina crucibles by the flux method increased, possibly caused by the partial incorporation of Al_2O_3 from the alumina crucible into the perovskite lattice to promote cell enlargement. Furthermore, when the Mg doping was less than 1 %, the lattice constant gradually increased because Mg preferentially replaced Ti, and the ionic radius of Mg^{2+} (0.72 Å) is larger than that of Ti^{4+} (0.61 Å) [48,49]. In addition, the lattice constant gradually decreased when the Mg^{2+} doping was 2 % and 3 % because the excess Mg^{2+} replaced Sr^{2+} (1.18 Å) [48]. The main reason for this phenomenon is that Sr^{2+} has a larger atomic radius, making the Sr-O bonds longer than the Mg-O bonds and thus more prone to breakage and substitution by Mg-O bonds [50].

The microstructure of the prepared samples was investigated by SEM and TEM. As shown in Fig. S6, pure STO had an amorphous shape, 0 % Mg-AlSTO and 1 %Mg-AlSTO became cubic after flux treatment, and some crystal facets were exposed at the same time [51]. These crystal
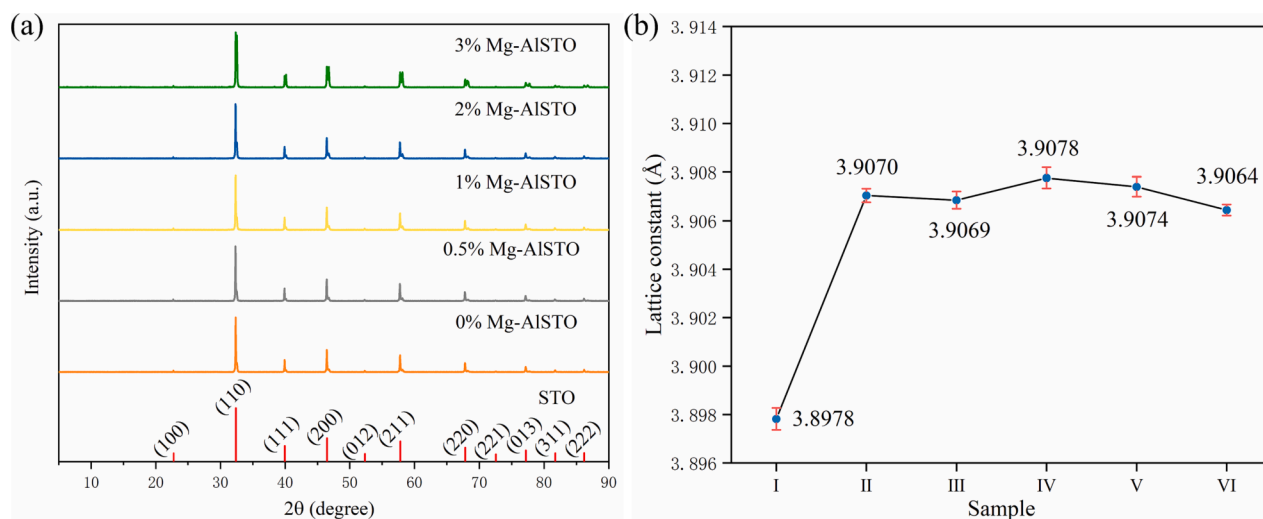
Fig. 1. (a) XRD patterns of the as-prepared catalysts; (b) lattice constant value [(I) STO, (II) 0 % Mg-AlSTO, (III) 0.5 % Mg-AlSTO, (IV) 1 % Mg-AlSTO, (V) 2 % Mg-AlSTO (VI) 3 % Mg-AlSTO].
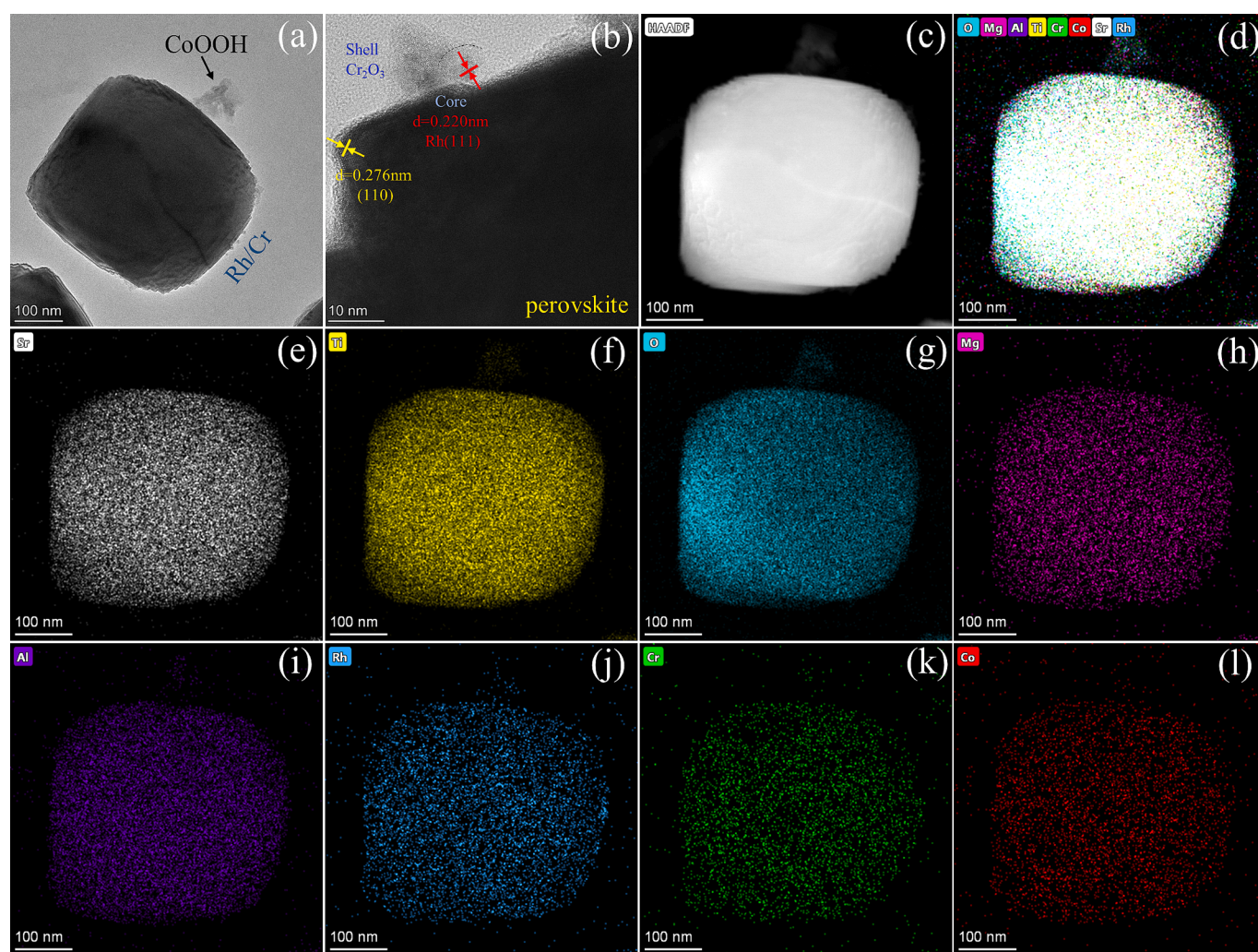
Fig. 2. Transmission electron microscopy image (a), HRTEM image of a 1 %Mg-AlSTO particle loaded with Rh (0.1 %wt)/Cr (0.05 %wt)/Co (0.05 %wt) (b); (e-l) EDS elemental mappings (strontium (Sr), titanium (Ti), oxygen (O), magnesium(Mg), aluminum (Al), Rh (rhodium), Cr (chromium) and Co (cobalt)) of the selected particle in (c) and (d).

facets were favorable to the loading of the cocatalyst, and the catalytic activity of the catalyst with more exposed crystal facets was significantly improved. As shown in Fig. S7a-c, the cocatalyst was firmly attached to the surface of 1 %Mg-AlSTO by photodeposition. As Fig. 2a shows, Rh/Cr_2O_3 and CoOOH were dispersed on the surface of the $SrTiO_3$ particles, and the lattice spacing of 0.276 nm displayed in Fig. 2b corresponded to the (1 1 0) crystal facets of perovskite $SrTiO_3$ [52], consistent with the XRD results. In addition, the loading form of the cocatalyst was further understood from Fig. 2b, which shows that these particles possessed a core–shell structure with an inner layer of Rh metal and an outer layer of Cr_2O_3. The lattice spacing of 0.220 nm corresponded to the (1 1 1) crystallographic plane of Rh, confirming the presence of a Rh core layer. Rh nanoparticles were reduced in situ by photoexcited electrons in $SrTiO_3$ during the photodeposition process, and the Cr_2O_3 wrapped around the Rh prevented the recombination of H_2 and O_2 at the Rh active site [51,53], ensuring the effective generation of hydrogen and oxygen and thus enhancing the photocatalytic water splitting activity. In addition, the EDS elemental scan images obtained within the selected area are shown in Fig. 2e-l. Sr, Ti, O, Mg, and Al were uniformly distributed in the nanoparticles, indicating the successful preparation of perovskite-type Mg-AlSTO. Rh, Cr, and Co were uniformly distributed on the surface of the nanoparticles and had a density much less than that of the aforementioned elements, revealing that a small amount of cocatalyst was needed for successful loading.

To further clarify the loading of the cocatalysts, ICP analysis was performed on 1 %Mg-AlSTO. As shown in Table S2, the contents of Rh, Cr, and Co were 0.082 wt%, 0.024 wt%, and 0.048 wt%, respectively, which were closer to the contents of the added elements.

The metal content of the prepared samples was measured by ICP. As displayed in Fig. S8, the Mg content increased linearly with the initial addition of a standard molar amount of MgO. The presence of Al was due to the diffusion of the alumina crucible into STO under high-temperature melting, and notably, the Al content gradually decreased with increasing Mg content, indicating that the presence of additional doping elements may have reduced the diffusion of Al_2O_3 in the crucible during the fluxing process.

The surface chemical composition and electronic state of the catalysts were investigated by XPS. As shown in the XPS spectra in Fig. S9, characteristic signal peaks corresponding to the Mg 1 s, O 1 s, Ti 2p, C 1 s, and Sr 3d regions were observed. The high-resolution O 1 s spectra of pure STO, 0 % Mg-AlSTO, and 1 % Mg-AlSTO are presented in Fig. S10. The prominent peak in the spectrum of perovskite $SrTiO_3$, with a binding energy of 529.5 eV, was assigned to lattice oxygen (O_{lat}), while the peak with a binding energy of 531.6 eV was attributed to adsorbed oxygen (O_{ads}), such as hydroxyl groups on the particle surface [48,54]. The concentration of surface oxygen vacancies was estimated from the ratio of adsorbed oxygen to lattice oxygen measured by XPS [55], and the calculation results are given in Table S3. The partial dissociation of Ti-O bonds in pure STO caused the absence of a small amount of lattice oxygen and thus the formation of oxygen vacancies [56], and the ratio of adsorbed oxygen to lattice oxygen for 0 % Mg-AlSTO was 0.80, which was significantly higher than that of 0.67 for pure STO. This was caused by the doping of Al^{3+} in the crucible into $SrTiO_3$ in the flux method, which promoted the formation of oxygen vacancies. When additional Mg^{2+} was introduced, the R value of 1 % Mg-AlSTO further increased to 0.86 because the ionic radii of Mg^{2+} and Ti^{4+} were similar, and Mg^{2+} partially replaced Ti^{4+}, further forming additional oxygen vacancies, which was consistent with a previous study that reported that doping with low-valent cations introduced oxygen defects [40]. Furthermore, the increase in surface oxygen vacancies provided more adsorption sites for H_2O molecules, enhancing the activity of photocatalytic water splitting [57]. To demonstrate that the introduction of surface oxygen vacancies could enhance the adsorption of water molecules, the catalysts were tested for water vapor adsorption by BET. Fig. S11 showed that pure STO had the lowest water adsorption, while 1 %Mg-AlSTO had the highest water adsorption. This was because 1 %Mg-AlSTO has the

highest content of surface oxygen vacancies, which can further enhance the adsorption of water molecules by the catalyst, which corroborates the results of the XPS analysis.

The high-resolution Sr 3d versus Ti 2p spectra of pure STO, 0 % Mg-AlSTO, and 1 % Mg-AlSTO are shown in Fig. S12. The binding energies of the Sr and Ti peaks of both samples were slightly shifted in a lower direction compared to the pure STO, which indicated that the doping of the Mg and Al elements brought some effect on the crystals [58,59]. This may be because Mg and Al doping into the STO lattice provide excess electrons. Furthermore, ESR characterization was used to determine the Ti^{3+} defect content [60]. As illustrated in Fig. S10b, pure STO had a high Ti^{3+} defect content, as determined from the intensity of the peak located at 1.976 [48], and the Ti^{3+} content decreased upon additional doping with Mg and Al because Mg^{2+} and Al^{3+} replaced part of the Ti^{3+} and Ti^{4+} at the same time, c ausing the Ti^{3+} defect content to decrease while increasing the content of oxygen defects, thus improving the water splitting activity of the catalyst. The XPS of Al 2p and Mg 1 s of 1 % Mg-ASTO showed a single peak at 74.22 eV and 1303.96 eV in Fig. S13, respectively, indicating the distribution of Al and Mg in the sample. To verify the stability of CoOOH, XPS characterization of the Co 2p of the catalysts before and after the reaction was performed. As shown in Fig. S14, the Co $2p_{3/2}$ peak at 780.47 eV and the Co $2p_{1/2}$ peak at 795.67 eV correspond to Co(III), while the Co $2p_{3/2}$ peak at 783.08 eV and the Co $2p_{1/2}$ peak at 798.24 eV correspond to Co(II). The total Co intensities of Co(III) and Co(II) on CoOOH were 72.73 % and 27.27 %, respectively, before the catalytic reaction, while the relative proportions of Co(III) and Co(II) were 72.26 % and 27.74 %, respectively, after the catalytic reaction. This indicated that CoOOH was stable during the hydrolysis reaction.

3.2. Experimental performance of photothermal catalysis by $SrTiO_3$ catalysts

Under xenon lamp irradiation ($\lambda > 320$ nm, Fig. S4a), the yields of H_2 and O_2 in the photothermal catalytic water splitting of STO samples were accurately measured, and the spectral distribution and intensity of the xenon lamp at the reaction position are presented in Fig. S2 and Table S4. As seen in Fig. 3a-b, the ratio of hydrogen to oxygen from the photothermal catalytic water splitting of all samples was close to 2:1, indicating that the catalyst had a good overall water splitting performance. The yields of hydrogen and oxygen in pure STO samples were 5.40 mmol·g^{-1}·h^{-1} and 2.85 mmol·g^{-1}·h^{-1}, respectively. When Al^{3+} was introduced into the crucible, the yields of hydrogen and oxygen increased to 19.97 mmol·g^{-1}·h^{-1} and 9.59 mmol·g^{-1}·h^{-1}, respectively, which proved that Al^{3+} doping had a positive effect on water splitting. Then, upon doping with additional Mg^{2+}, the yields of hydrogen and oxygen were 37.72 mmol·g^{-1}·h^{-1} and 18.32 mmol·g^{-1}·h^{-1} (0.5 % Mg-AlSTO), 51.55 mmol·g^{-1}·h^{-1} and 25.59 mmol·g^{-1}·h^{-1} (1 % Mg-AlSTO), 40.98 mmol·g^{-1}·h^{-1} and 20.21 mmol·g^{-1}·h^{-1} (2 % Mg-AlSTO), and 38.55 mmol·g^{-1}·h^{-1} and 18.10 mmol·g^{-1}·h^{-1} (3 % Mg-AlSTO), among which 1 % Mg-AlSTO exhibits the best water splitting activity and hydrogen production. The activity was approximately 9.5 times that of pure STO. To further confirm the validity of Mg, Al codoping, water decomposition experiments were performed on $SrTiO_3$ doped with single Mg or Al elements. As shown in Fig. S15, the pristine STO had the lowest activity, and the water decomposition activity was further enhanced when Mg or Al elements were doped in $SrTiO_3$. However, when Mg, Al codoping were used, the water decomposition activities were all higher than the yields of single doping. These results confirmed that the codoping of Mg^{2+} and Al^{3+} can effectively enhance the water splitting activity.

The thermal effect-induced temperature increase had an important effect on the photothermal catalytic water splitting reaction, as shown in Fig. 3c. A control experiment was carried out for 1 % Mg-AlSTO loaded with cocatalysts. When using a light source that filtered out 700 nm for the catalytic reaction, the hydrogen and oxygen yields were reduced by
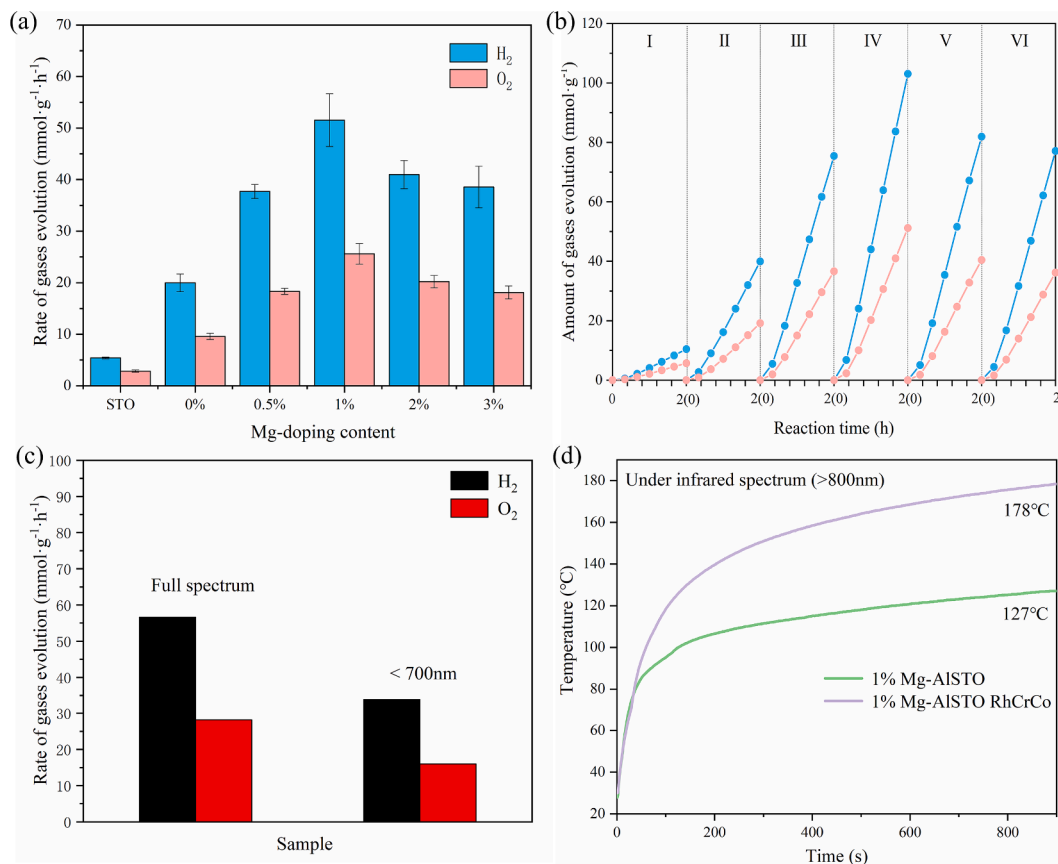
Fig. 3. Corresponding H_2 and O_2 production rates (a), the typical time course of H_2 and O_2 evolution (b) over the as-prepared catalysts loaded with Rh (0.1 %wt)/Cr (0.05 %wt)/Co (0.05 %wt). Corresponding H_2 and O_2 production rates of 1 % Mg-AlSTO loaded with Rh (0.1 % wt)/Cr (0.05 %wt)/Co (0.05 %wt) under different light sources (Sample I:full spectrum; and II: < 700 nm) (c). Temperature variation curve with time under infrared spectrum irradiation (>800 nm) (d).

40 % compared to those determined from the full spectrum. This was probably because infrared light has a strong thermal effect in the solar spectrum, effectively increasing the temperature of the reaction system. When only the spectrum below 700 nm was considered, the reaction temperature decreased, which affected the water splitting reaction. At the same time, the non-100 % transmittance of the filter was also an influencing factor. As shown in Table S5, filters can cause about 13.5 % attenuation of light intensity, which can cause a decrease in part of the water decomposition activity. Since the photothermal conversion characteristics of the catalyst significantly affected the photothermal catalytic activity, the infrared spectrum (>800 nm) with the most obvious thermal effect was selected as the simulated light source, and the surface temperature of the sample was monitored by a thermocouple. As shown in Fig. 3d, the temperature of both samples increased rapidly at the moment the light was turned on and then stabilized. The final temperature of 1 % Mg-AlSTO with a cocatalyst increased by 51 °C,
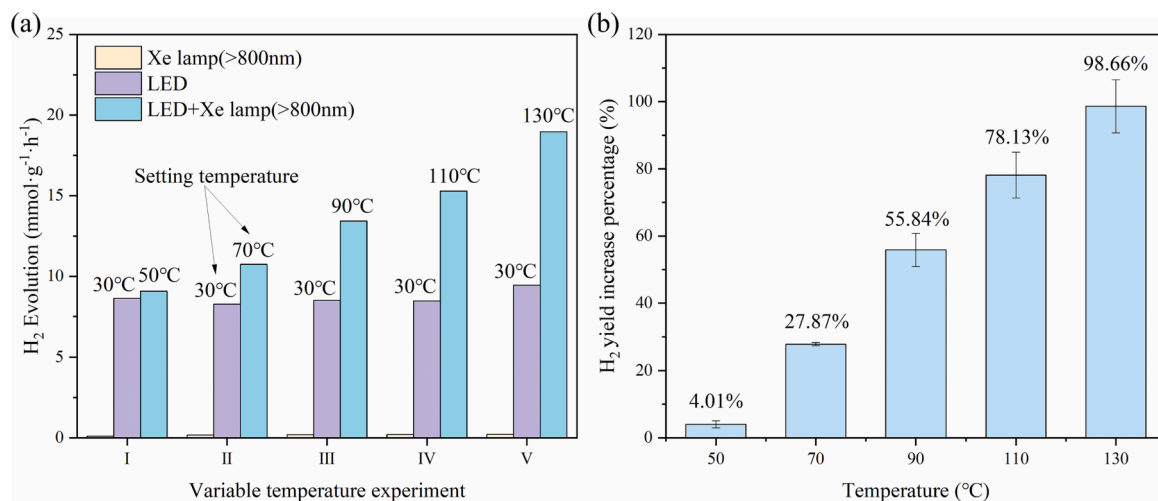
Fig. 4. (a) Hydrogen production rates of 1 %Mg-AlSTO loaded with Rh (0.1 %wt)/Cr (0.05 %wt)/Co (0.05 %wt) at different temperatures (30–130 ℃). (b) The percentage increase in the H_2 production rate at different temperatures compared to only turning on the LED (30 ℃).

revealing that Rh/Cr$_2$O$_3$ and CoOOH not only enhanced the photocatalytic activity but also had a strong photothermal effect that could further increase the reaction temperature.

To determine the influence of temperature caused by the thermal effect on the catalyst reaction activity, the following experiments were designed to investigate the photothermal catalytic water splitting reaction performance of 1 % Mg-AlSTO loaded with cocatalysts at different temperatures. The catalytic reaction mode is shown in Fig. S1b. A 365 nm LED was used for the water splitting reaction, while an 800 nm cutoff filter was employed to filter the xenon lamp to ensure that only infrared light was transmitted to heat the catalytic reaction. As seen in Fig. 4a, there was a small amount of H$_2$ production when only the xenon lamp was turned on for irradiation, probably because the 800 nm cutoff filter had a small amount of short-wavelength spectral leakage. When only the 365 nm LED was turned on, H$_2$ production began to increase due to the strong absorption of 1 % Mg-AlSTO in the ultraviolet band. After the LED lamp was illuminated for a period of time, the xenon lamp was turned on to heat the sample to the set temperature by the thermal effect of infrared light, the hydrogen increased as the temperature increased by 4.01 % (50 °C), 27.87 % (70 °C), 55.84 % (90 °C), 78.13 % (110 °C), and 98.66 % (130 °C). With the synergistic interaction of the photoeffect and thermal effect, the H$_2$ yield increased from 9.44 mmol·g^{-1}·h^{-1} under pure photocatalytic conditions to 19.97 mmol·g^{-1}·h^{-1}, a nearly twofold

increase. Several experiments at each temperature are shown in Fig. S16 to ensure good reproducibility of the experimental results. The growth trend of oxygen production with temperature is similar to that of hydrogen production, as shown in Fig. S17. The above results proved that utilizing the good thermal effect of the infrared spectrum to elevate the temperature can effectively enhance the H$_2$ production, therefore, combining the light effect with the thermal effect in an effective way can improve the conversion and utilization of solar energy.

3.3. Characterization of the optical properties

The optical properties of the prepared catalysts were investigated by UV–vis absorption spectroscopy, as shown in Fig. 5a. The intrinsic absorption edges in the spectra of all the samples were located at approximately 380 nm, and the remaining samples showed significantly enhanced light absorption in the UV and visible regions compared to pure STO. Based on the Kubelka-Munk theory [61], the band gaps of all the samples were calculated to be approximately 3.28 eV and did not change significantly with the doping of Al^{3+} and Mg^{2+}. It is well known that the conduction band (CB) and valence band (VB) of SrTiO$_3$ depend on the unoccupied Ti 3d orbitals and the occupied O 2p orbitals, respectively [62]. The above results indicate that the codoping of Al^{3+} with Mg^{2+} in SrTiO$_3$ effectively enhanced the photoeffect of the catalyst.
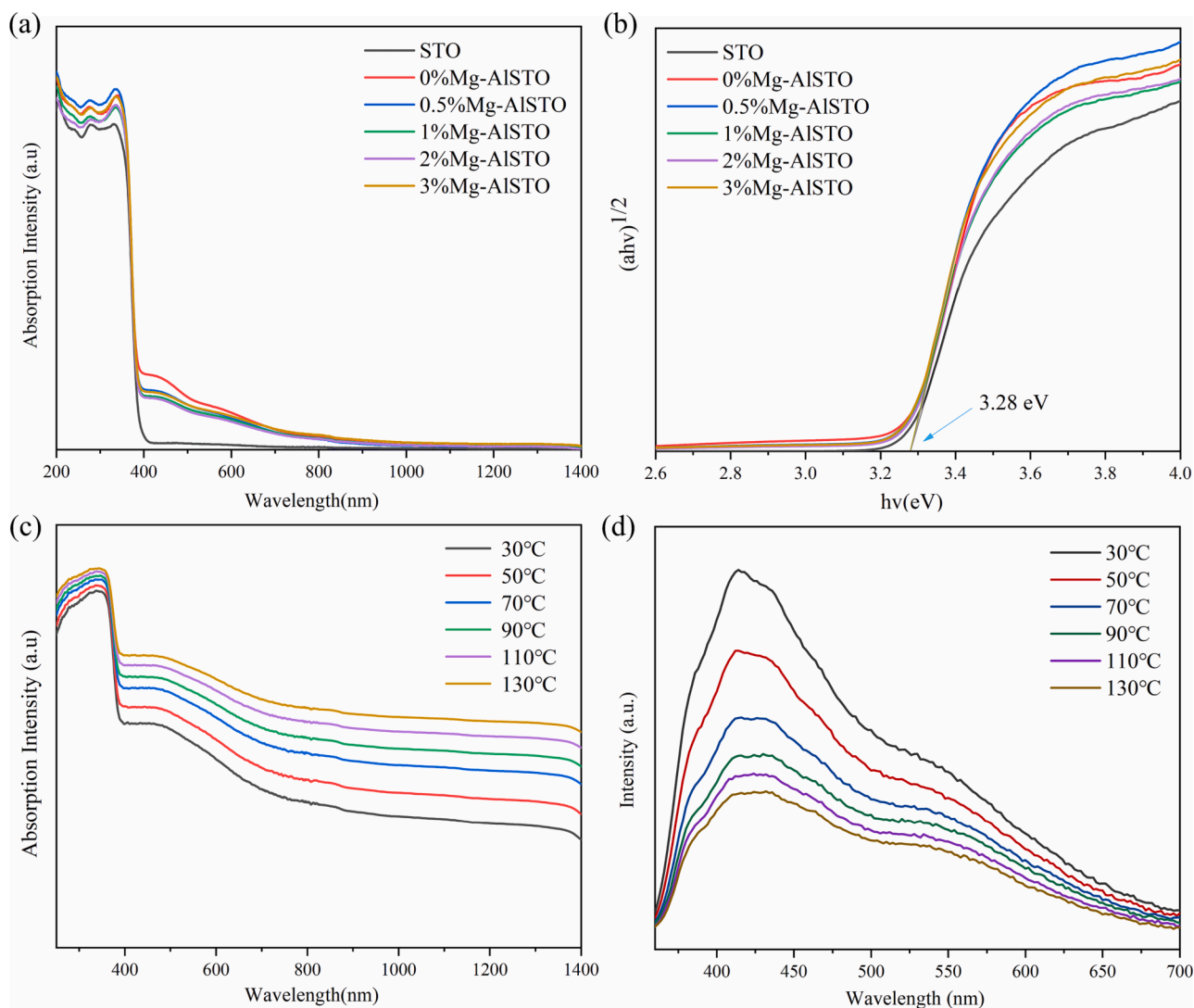
Fig. 5. (a) UV–vis absorption spectra and (b) determination of the optical band gap over as-prepared catalysts. (c) UV − Vis diffuse reflectance spectra and (d) PL spectra of 1 %Mg-AlSTO loaded with Rh (0.1 % wt)/Cr (0.05 % wt)/Co (0.05 % wt) at different temperatures.

The photogenerated carrier recombination of the prepared catalysts was probed using PL. The main peak at 435 nm was attributed to an inter-band transition in $SrTiO_3$ where excited electrons from the conduction band return to the valence band to emit photons. The small peak at 532 nm was attributed to oxygen defects in $SrTiO_3$ [63,64]. These defects created defect energy levels between the valence and conduction bands, resulting in longer wavelength emission peaks. Compared to that of pure STO, the radiation intensity of the material upon the introduction of Al^{3+} was enhanced, as seen from the UV–vis spectra, which could be attributed to the enhanced light absorption of this sample, resulting in similarly enhanced radiation recombination. Interestingly, when Mg^{2+} was further introduced, the radiation intensity of the sample gradually decreased, indicating that the photogenerated carrier recombination gradually decreased, which was favorable for the activity of the photothermal catalytic water splitting reaction. In addition, the doped catalyst showed enhanced absorption in the visible region. According to prior literature, this was often linked to the existence of defects [65,66]. When $SrTiO_3$ was doped with low-valence cations like Mg^{2+} or Al^{3+}, they substituted Ti^{3+} and created more oxygen vacancies. This might explain the extended absorption region for visible light in the materials. As observed in Fig. 5a, the bandgap for all materials was 3.28 eV, suggesting that the inclusion of Mg^{2+} and Al^{3+} did not cause a notable change in the bandgap of $SrTiO_3$. As seen from Fig. S18, the lowest radiation intensity, which corresponded to the highest yield in the experimental results, was observed for 1 % Mg-AlSTO.

The study of the radiation absorption properties of semiconductors due to temperature induced by the photothermal effect is important for facilitating the conversion of solar energy into hydrogen energy [67]. To further explore the light absorption of the material and the change in the energy band with temperature, UV–vis absorption spectroscopy of 1 % Mg-AlSTO RCC (with Rh, Cr, and Co) at different temperatures was performed. As shown in Fig. 5c, the shape of the light absorption curve of the material did not change significantly in the temperature interval of 30-130°C, indicating that the structure of the catalyst did not obviously change in this temperature range. Notably, the light absorption of the catalytic material in the ultraviolet band was enhanced with increasing temperature, consistent with the experimental results. When using a xenon lamp that filters out wavelengths below 800 nm and uses only infrared light to provide a heat source to raise the temperature, the absorption of the catalytic material in the ultraviolet region (365 nm LED) was effectively improved, which increased the yield of water splitting. At the same time, the increase in temperature caused the absorption edge of the material to be redshifted, which expanded the spectral absorption range of 1 % Mg-AlSTO RCC [68], and the increase in temperature enhanced the absorption of visible and infrared light more significantly than that of ultraviolet light. This may be one of the reasons why 1 % Mg-AlSTO with the cocatalyst had good photothermal conversion ability. Overall, the temperature increase due to the photothermal effect promoted the light absorption capacity of the material for the full spectrum, which was beneficial to the solar photothermal water splitting reaction. As shown in Fig. S19, based on the Kubelka-Munk theory, the band gap variation of 1 % Mg-AlSTO RCC with temperature was calculated to be 3.13 eV at 30 °C, which is smaller than the value of 3.28 eV previously calculated from the UV spectrum, presumably because the loading of the cocatalyst changed the band gap. As the temperature increased, the band gap of 1 % Mg-AlSTO RCC gradually narrowed, reaching 3.03 eV at 130 °C, which is 0.1 eV smaller than the band gap at 30 °C (3.13 eV). This may be due to the increased electron–phonon interaction caused by the increase in temperature, which intensified the lattice vibration and lattice expansion, thus shifting the energy band of the semiconductor material and resulting in a smaller band gap, which can generate more photogenerated carriers.

The PL spectra of 1 % Mg-AlSTO RCC at different temperatures were obtained to explore the effect of temperature on the radiative complexation of photogenerated carriers. Fig. 5d shows that the PL of the sample gradually decreased with increasing temperature, indicating

that an increase in temperature reduced the radiative recombination of photogenerated carriers. Therefore, at higher temperatures, photogenerated carriers more effectively migrated to the cocatalyst on the catalyst's surface to prolong the lifetime and inhibit the recombination of electrons and holes, which further improved the catalytic efficiency of the photocatalysts for water splitting [26].

To gain insight into the performance of the catalyst at different temperatures, the variation in the photocurrent with temperature over time was first measured for 1 % Mg-AlSTO RCC. Because of the temperature limitation of the solution, the maximum temperature was chosen to be 90 °C. As illustrated in Fig. 6a, the peak was due to the large instantaneous photocurrent generated at the moment the light was turned on; as the light irradiation time increased, the electron transfer rate of the semiconductor material tended to stabilize and gradually become flat. The catalyst transient photocurrent increased significantly with increasing temperature, and the photocurrent density was improved nearly eightfold when the temperature was changed from 30 to 90 °C. When performing photocurrent experiments at different temperatures, it was important to consider the change in the resistance of the electrolyte. Fig. S20 showed that the resistance of the electrolyte (0.5 M Na_2SO_4) steadily decreased as the temperature increased, resulting in a corresponding increase in the photocurrent.

The impedance of the high-frequency band in the EIS test was mainly dominated by the carrier migration resistance [69]. The radius of the high-frequency band of the curve decreased with temperature from 30 to 130°C, as shown in the EIS plot (Fig. 6b), implying that the electrical impedance of 1 % Mg-AlSTO RCC decreased with increasing temperature [70]. This indicated that an increase in temperature significantly reduced the photogenerated carrier mobility resistance, which may be one of the reasons for the temperature-dependent increase in the photocurrent density of the material. In addition, for semiconductors, the resistance was negatively correlated with temperature in a certain interval since the free electrons in the metal vibrated more at higher temperatures, resulting in a positive temperature dependence of the resistance of the metal. When the temperature increased, the arc radius of 1 % Mg-AlSTO RCC still decreased, indicating that the change in EIS of the material mainly originated from the decrease in the resistance of the semiconductor 1 % Mg-AlSTO.

A Mott-Schottky curve of a material provides information about the semiconductor type as well as the flat-band potential [71]. As shown in Fig. 6c, the slope of the curve for 1 % Mg-AlSTO RCC was positive at all test temperatures, which indicated that this material was an n-type semiconductor. Its flat band potentials at 30 °C, 50 °C, 70 °C, and 90 °C were −0.76, −0.88, −0.90, and −0.98 V (vs. Ag/AgCl), namely −0.56, −0.68, −0.70, and −0.78 V (vs. NHE). The flat band potential can be approximated as the conduction band (CB) of the photocatalyst [72–74]. On the basis of the calculation results of the UV–vis spectral band gap, the energy band structure of the catalyst, as it changed with temperature, was determined. As Fig. 6d shows, the CB potential of 1 % Mg-AlSTO RCC shifted to a more negative potential direction with increasing temperature, which improved the reduction ability of the photogenerated electrons and made the material more suitable for the hydrogen evolution reaction. The valence band also shifted to a lower potential but remained higher than the oxygen production potential in the 30–90 °C range, allowing the catalyst to maintain a strong ability with overall water splitting capability. Therefore, the shift of the energy band may be one of the reasons for the improvement in water splitting performance with increasing temperature.

3.4. Mechanism of photothermal synergistic reaction

The chemical reaction in photothermal catalytic water splitting was further investigated by DFT calculations, and the established $SrTiO_3$ model (1 0 0) is shown in Fig. S3. Since oxygen vacancies are easily generated in the lattice of Mg^{2+}- and Al^{3+}- doped $SrTiO_3$ by the flux method, the oxygen vacancy formation energies around the doped metal
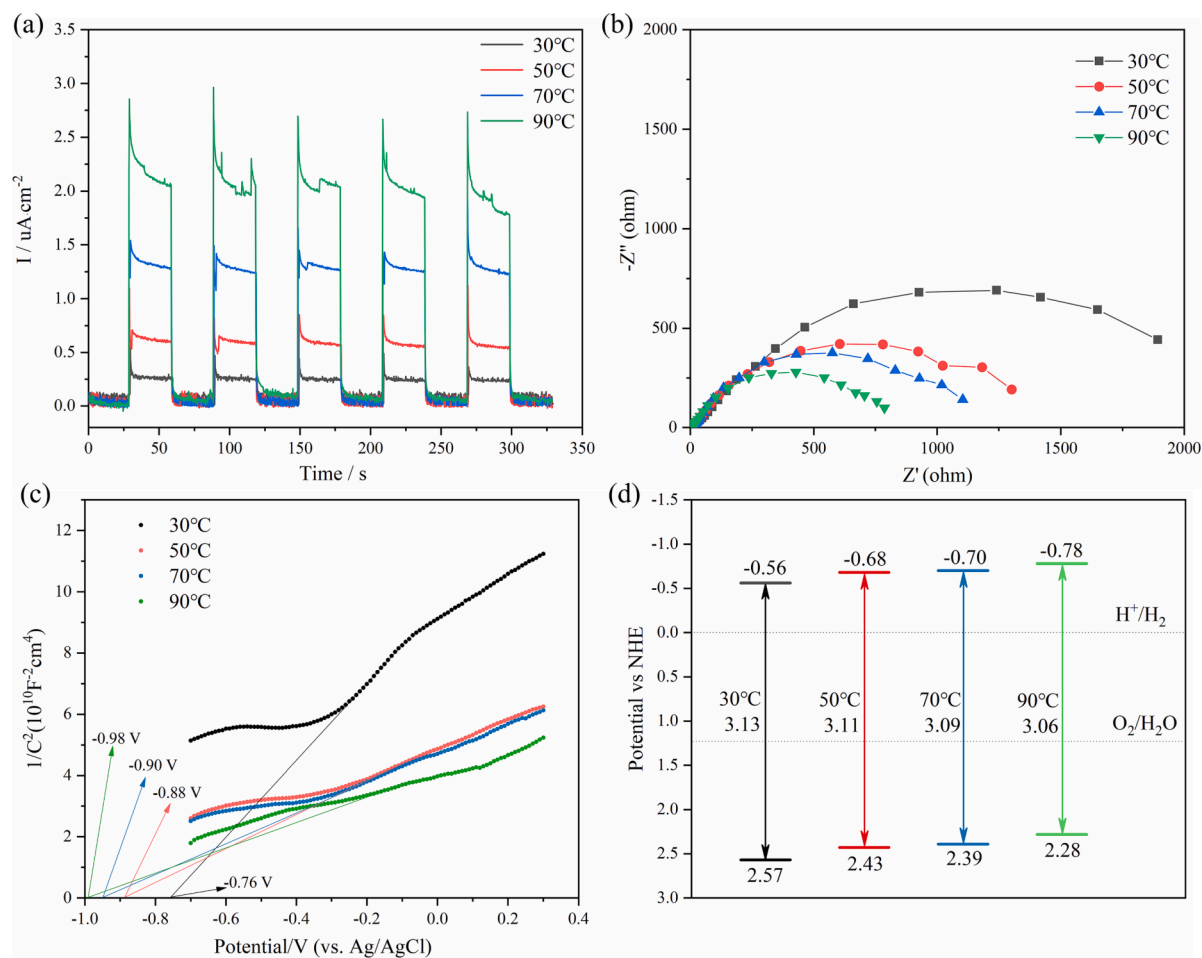
Fig. 6. (a) Time-dependent photocurrent result, (b) EIS change, (c)MS curves, and (d) energy band structure of 1 % Mg-AlSTO loaded with Rh (0.1 %wt)/Cr (0.05 % wt)/Co (0.05 %wt) at different temperatures.
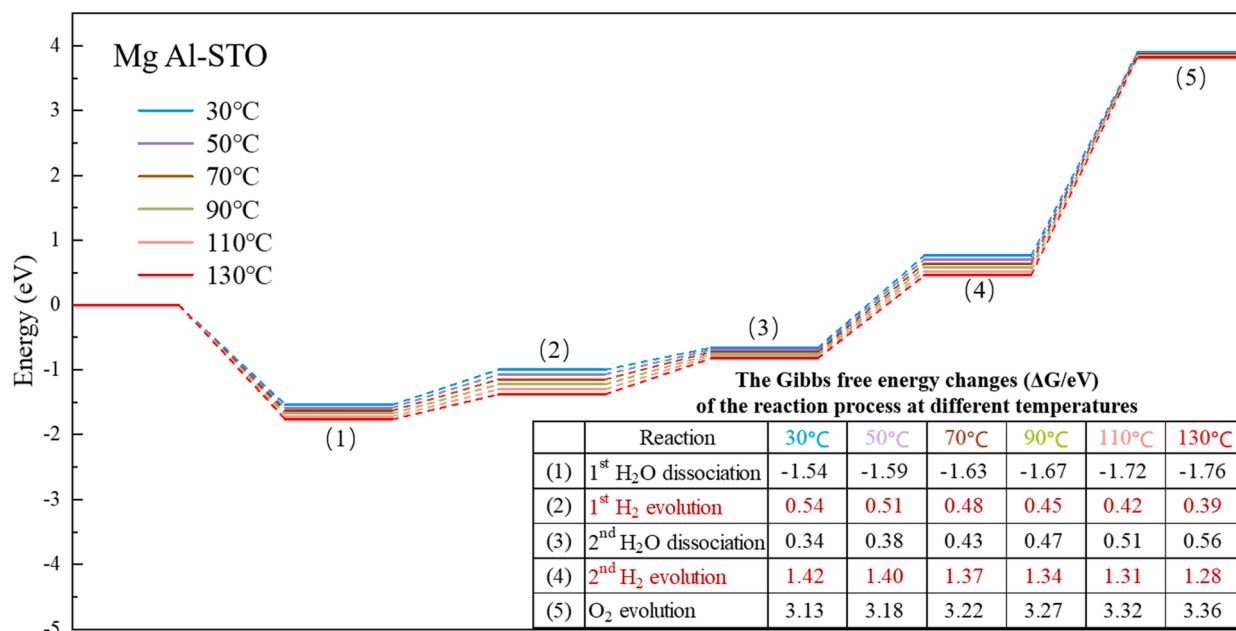
Fig. 7. Gibbs free energy of the water splitting reaction path on Mg, Al codoped $SrTiO_3$ loaded with Rh clusters at different temperatures.

The Gibbs free energy changes (ΔG/eV) of the reaction process at different temperatures

	Reaction	30°C	50°C	70°C	90°C	110°C	130°C
(1)	1st H_2O dissociation	-1.54	-1.59	-1.63	-1.67	-1.72	-1.76
(2)	1st H_2 evolution	0.54	0.51	0.48	0.45	0.42	0.39
(3)	2nd H_2O dissociation	0.34	0.38	0.43	0.47	0.51	0.56
(4)	2nd H_2 evolution	1.42	1.40	1.37	1.34	1.31	1.28
(5)	O_2 evolution	3.13	3.18	3.22	3.27	3.32	3.36

sites were first calculated. As shown in Fig. S21 and Table S6, oxygen vacancies were most likely to form at positions adjacent to Al and perpendicular to the Mg-Al bond. The adsorption energies of H_2O at different sites on the surface of $SrTiO_3$ (1 0 0) were further calculated, and the results in Table S7 indicate that water molecules prefer to adsorb at interfaces with oxygen vacancies, which proves that the introduction of oxygen vacancies in $SrTiO_3$ provided more adsorption sites for water splitting reactions.

Based on previous work [75], a water splitting reaction pathway with oxygen vacancies present on the initial surface of the $SrTiO_3$-based catalyst was established, as illustrated in Fig. S22; This pathway contained five key steps of the photothermal water splitting reaction. Initially, water molecules were adsorbed on the oxygen vacancies on the surface; then, they decomposed into hydroxyl groups and hydrogen atoms [* (V_o) + H_2O → *$OH(V_o)$ + *H]. Subsequently, the H atom in OH groups was dissociated and coupled with the previously generated H atom to form H_2, which was desorbed, and the O atom in OH groups temporarily occupied the oxygen vacancy (*$OH(V_o)$ + *H → * + H_2↑). Furthermore, the second water molecule was adsorbed and desorbed, leaving hydroxyl groups, hydrogen atoms, and previous oxygen atoms on the surface (* + * (V_o) + H_2O → * + *$OH(V_o)$ + *H). Afterward, a second hydrogen was produced, and a second oxygen atom was connected to the oxygen on the oxygen vacancies (* + *$OH(V_o)$ + *H → *O-$O(V_o)$ + H_2↑). Oxygen was produced in the final step and regenerated the oxygen vacancies (*O-$O(V_o)$ → * (V_o) + O_2↑).

In the photothermal catalytic water splitting reaction with solar energy as the sole energy source, the thermal effect caused by radiation absorption by materials affects the energy barrier of the steps in the reaction. The Gibbs free energy of the catalyst was calculated for each step of the reaction between 30 and 130 °C as presented in Fig. 7. As the temperature increased, the water adsorption energy barrier of step (1) decreased, which means that the initial adsorption of water on the catalyst surface increased. In contrast, the water adsorption energy barrier of step (3) increased with increasing temperature, indicating that the second water molecule adsorbed on had a weaker ability to bind to the oxygen that had filled the initial oxygen vacancies, suggesting that the presence of the oxygen vacancies effectively enhanced the adsorption of water molecules. More importantly, the energy barriers for H_2 production and desorption in steps (2) and (4) decreased with increasing

temperature, indicating that H_2 was more easily produced and desorbed at high temperatures, which explains the gradual increase in H_2 yield with increasing temperature in the experiment. Finally, the elevated temperature raised the energy barrier for O_2 evolution in step (5), but the overall trend of the curves in the figure shows that O_2 evolution and desorption are favorable at higher temperatures. In summary, the enhancement of the radiant thermal effect can effectively enhance the activity of the photothermal catalytic water splitting reaction.

Based on the above analysis, it was concluded that the outstanding water splitting reaction activity of 1 % Mg-AlSTO with cocatalysts was due to synergism between the photoeffect and thermal effect, and the photothermal synergistic reaction mechanism is shown in Fig. 8. On the one hand, from the perspective of the photoeffect of the material, the introduction of Al^{3+} into $SrTiO_3$ effectively reduced the Ti^{3+} content and increased the concentration of oxygen vacancies [56]. In addition, the introduction of Mg^{2+} further increased the concentration of oxygen vacancies, resulting in enhanced adsorption of water molecules. It also broadened the spectral absorption range of the material and reduced the radiative recombination of photoexcited carriers. Furthermore, by loading the hydrogen-generating cocatalyst Rh/Cr_2O_3 and the oxygen-generating cocatalyst CoOOH, the photogenerated electron-hole pair transfer of $SrTiO_3$ was effectively improved, thereby greatly enhancing the photocatalytic water splitting ability of $SrTiO_3$. When Rh and $SrTiO_3$ are in contact, a Schottky junction is formed, which effectively promotes the transfer of electrons from the semiconductor $SrTiO_3$ to Rh to participate in the reaction, and the further deposition of Cr_2O_3 forms a core–shell structure with Rh, which prevents O_2 from coming into contact with Rh and does not interfere with the transfer of H^+, thus reducing the reverse reaction of water splitting [53,76,77]. CoOOH is an effective hole extractor that promotes the effective separation of electrons and holes, which prevents Cr^{3+} from being oxidized by oxygen during the reaction, further increasing the yield of the water splitting reaction [78]. At the same time, these cocatalysts exhibit strong photothermal effects. Temperature measurements showed that the surface temperature of the 1 % Mg-AlSTO material loaded with $Rh/Cr_2O_3/$CoOOH cocatalysts increased by 51 °C compared to that of 1 % Mg-AlSTO alone. Fig. 3c clearly shows the crucial role of the infrared-induced thermal effect in further increasing the performance of water splitting. Therefore, spectroscopic experiments and temperature-
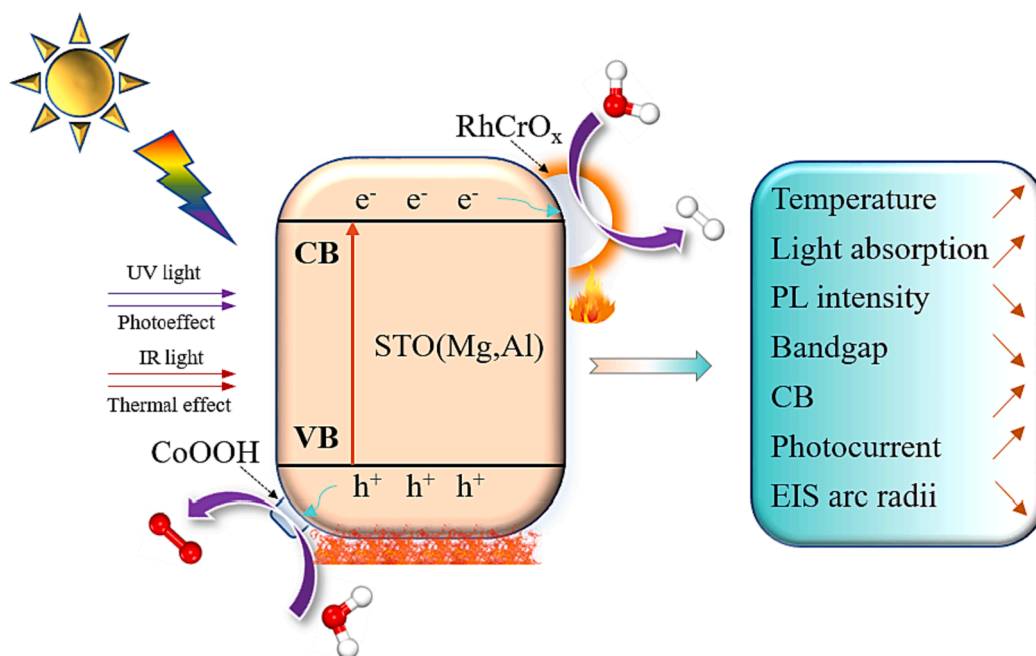

Fig. 8. Mechanism diagram of photothermal catalytic water splitting over Mg, Al codoped $SrTiO_3$ loaded with Rh /Cr_2O_3 /CoOOH.

dependent characterizations were conducted to investigate in detail the influence of thermal effects on water splitting productivity. For the 1 % Mg-AlSTO loaded with cocatalysts, increasing the temperature enhanced the catalyst's overall light absorption across the solar spectrum. The improved ultraviolet absorption led to the generation of more photoexcited charge carriers. In addition, the improvements in the visible and infrared range further enhanced the photothermal effects of the catalyst, resulting in elevated surface temperatures. At the same time, the radiative recombination of photogenerated carriers was reduced with increasing temperature, which promotes carrier separation and allows for more photogenerated carriers to participate in the photothermal synergistic water splitting reaction. In this catalyst, the increase in temperature due to thermal effects has a positive influence on the light absorption intensity as well as the carrier behavior. The enhancement of spectral absorption and the reduction of carrier recombination are both favorable for improving hydrogen production [79]. The resistance of semiconductor materials gradually decreases with increasing temperature, facilitating the transfer of photogenerated electrons to the surface of the photocatalyst, and the energy band position of the material shifted slightly in the negative direction, endowing the photogenerated electrons with a stronger reduction ability, which is favorable for H_2 generation. The above analysis provides reasons for the gradual increase in the photothermal catalytic water splitting capability of the 1 % Mg-AlSTO RCC sample with increasing temperature induced by thermal effects. Therefore, the design of catalyst materials that combine optical and thermal effects is advantageous for significantly improving the performance of water splitting and promoting the effective utilization of solar energy.

4. Conclusion

In conclusion, the dual strategy of using codoping and coloading in $SrTiO_3$ achieved a photothermal synergistic effect and effectively enhanced the yield of photothermal catalytic water splitting. A total of 51.55 mmol·g^{-1}·h^{-1} H_2 and 25.59 mmol·g^{-1}·h^{-1} O_2 were generated by loading Mg-Al-codoped $SrTiO_3$ with Rh/Cr_2O_3/CoOOH under the photothermal synergistic reaction. The introduction of Mg^{2+} and Al^{3+} into $SrTiO_3$ increased the oxygen vacancy concentration, increased the absorption range for the solar spectrum, and reduced the radiative recombination of carriers, which efficiently strengthened the optical response of $SrTiO_3$. After further loading the commonly used cocatalysts Rh/Cr_2O_3 and CoOOH, a dual synergistic photo and thermal effect was realized. It not only promoted the effective migration of photogenerated carriers but also induced a significant thermal effect, which promoted the water splitting reaction process by increasing the surface temperature. Spectroscopic experiments demonstrated that under the synergism of the photoeffect and the thermal effect, the H_2 yield was enhanced nearly twofold compared with that of the photocatalytic reaction alone. The characterization results showed that with an increase in temperature due to thermal effects, the photocurrent of the catalyst increased, the electrical impedance decreased, and the band gap narrowed, while the light absorption of solar light in the entire region was enhanced and the radiative recombination of carriers decreased. In addition, the energy band position shifted negatively with increasing temperature, resulting in a better performance of hydrogen production. The DFT calculations confirmed that elevated temperatures lowered the energy barrier at key steps in the reaction. These analyses illustrate the phenomenon that temperature has a positive correlation with the reaction activity of hydrogen evolution. Therefore, it is necessary to consider the interaction between the light effect and the thermal effect at the same time in solar energy utilization to further realize the efficient coupling of the two. This study holds significant importance in terms of the efficient utilization of solar energy and the design of synergistic photothermal catalysts.

CRediT authorship contribution statement

Xuan Zhu: Conceptualization, Methodology, Validation, Formal analysis, Investigation, Writing – original draft, Visualization. **Yan Liu:** Methodology, Software. **Menglin Wang:** Validation. **Li Zhang:** Methodology. **Qiaoli Li:** Data curation. **Entao Zhang:** Formal analysis. **Hongfen Mo:** Investigation. **Yuan Gao:** Conceptualization. **Chenyu Xu:** Writing – review & editing, Supervision. **Yanwei Zhang:** Resources, Project administration, Funding acquisition.

Declaration of competing interest

The authors declare that they have no known competing financial interests or personal relationships that could have appeared to influence the work reported in this paper.

Data availability

Data will be made available on request.

Acknowledgements

Appendix A. Supplementary data

Supplementary data to this article can be found online at https://doi.org/10.1016/j.cej.2023.147636.

References

[1] P. Wang, S. Fan, X. Li, J. Wang, Z. Liu, C. Bai, M.O. Tadé, S. Liu, Piezotronic effect and hierarchical Z-scheme heterostructure stimulated photocatalytic H_2 evolution integrated with C-N coupling of benzylamine, Nano Energy 89 (2021), 106349.

[2] H. Dong, T. Wang, X. Wang, F. Liu, C. Hou, Z. Wang, W. Liu, L. Fu, X. Gao, Humidity sensitivity reducing of moisture swing adsorbents by hydrophobic carrier doping for CO_2 direct air capture, Chem. Eng. J. 466 (2023), 143343.

[3] X. Ren, D. Philo, Y. Li, L. Shi, K. Chang, J. Ye, Recent advances of low-dimensional phosphorus-based nanomaterials for solar-driven photocatalytic reactions, Coord. Chem. Rev. 424 (2020), 213516.

[4] K.B. Parimi, B.S. Kaur, S.V.P. Lankapalli, J. Sagari, Performance, combustion, and emission characteristics of on a diesel engine fuelled with hydrogen compressed natural gas and Kusum seed biodiesel, Waste Dispos. Sustain. Energy 5 (2023) 151–163.

[5] J. Liu, Y. Xuan, L. Teng, Q. Zhu, X. Liu, Y. Ding, Solar-driven calcination study of a calcium-based single particle for thermochemical energy storage, Chem. Eng. J. 450 (2022).

[6] P. Wang, S. Song, M. He, C. Li, W. Wang, H. Li, X. Yuan, Z. Fang, K.P. Rinel, W. Song, J. Li, D.G. Vlachos, Z. Li, High-density defects in ordered macroporous-mesoporous CoNiFe-LDHs for efficient and robust oxygen evolution reaction, Chem. Catal. 3 (2023), 100497.

[7] W. Wang, S. Song, P. Wang, M. He, Z. Fang, X. Yuan, H. Li, C. Li, X. Wang, Y. Wei, W. Song, H. Xu, Z. Li, Chemical Bonding of g-C_3N_4/UiO-66(Zr/Ce) from Zr and Ce Single Atoms for Efficient Photocatalytic Reduction of CO_2 under Visible Light, ACS Catal. 13 (2023) 4597–4610.

[8] W.H. Lee, C.W. Lee, G.D. Cha, B.-H. Lee, J.H. Jeong, H. Park, J. Heo, M.S. Bootharaju, S.-H. Sunwoo, J.H. Kim, K.H. Ahn, D.-H. Kim, T. Hyeon, Floatable photocatalytic hydrogel nanocomposites for large-scale solar hydrogen production, Nat. Nanotechnol. (2023).

[9] H. Chen, L. Shao, C. Wang, Y. Fu, Construction of a hierarchical tubular metal–organic framework composed of nanosheet arrays as a photothermal catalyst through phase transformation, J. Mater. Chem. A 10 (2022) 17434–17439.

[10] Z. Wang, C. Li, K. Domen, Recent developments in heterogeneous photocatalysts for solar-driven overall water splitting, Chem. Soc. Rev. 48 (2019) 2109–2125.

[11] Z. Li, P. Wang, C. Ma, F. Igbari, Y. Kang, K.-L. Wang, W. Song, C. Dong, Y. Li, J. Yao, D. Meng, Z.-K. Wang, Y. Yang, Single-Layered MXene Nanosheets Doping TiO_2 for Efficient and Stable Double Perovskite Solar Cells, J. Am. Chem. Soc. 143 (2021) 2593–2600.

[12] J. Hong, C. Xu, B. Deng, Y. Gao, X. Zhu, X. Zhang, Y. Zhang, Photothermal Chemistry Based on Solar Energy: From Synergistic Effects to Practical Applications, Adv. Sci. 9 (2022) e2103926.

[13] A. Prasad, J. Verma, S. Suresh, S. Arisutha, Recent advancements in the applicability of SnO$_2$-based photo-catalysts for hydrogen production: challenges and solutions, Waste Dispos. Sustain. Energy 4 (2022) 179–192.

[14] J. Xu, W.-M. Yang, S.-J. Huang, H. Yin, H. Zhang, P. Radjenovic, Z.-L. Yang, Z.-Q. Tian, J.-F. Li, CdS core-Au plasmonic satellites nanostructure enhanced photocatalytic hydrogen evolution reaction, Nano Energy 49 (2018) 363–371.

[15] K. Malaie, Z. Heydari, M.R. Ganjali, Spinel nano-ferrites as low-cost (photo) electrocatalysts with unique electronic properties in solar energy conversion systems, Int. J. Hydrog. Energy 46 (2021) 3510–3529.

[16] D. Jin, F. Qiao, H. Chu, Y. Xie, Progress in electrocatalytic hydrogen evolution of transition metal alloys: synthesis, structure, and mechanism analysis, Nanoscale 15 (2023) 7202–7226.

[17] K. Dulta, A.O. Adeola, S.E. Ashaolu, T.I. Banji, J.O. Ighalo, Biohydrogen production and its bioeconomic impact: a review, Waste Dispos. Sustain. Energy 4 (2022) 219–230.

[18] L. Guo, C. Zhong, J. Cao, Y. Hao, M. Lei, K. Bi, Q. Sun, Z.L. Wang, Enhanced photocatalytic H$_2$ evolution by plasmonic and piezotronic effects based on periodic Al/BaTiO$_3$ heterostructures, Nano Energy 62 (2019) 513–520.

[19] W. Zeng, Y. Dong, X. Ye, G. Guan, T. Zhang, L. Guo, Ultrathin porous carbon nitride with molecular structure regulation for excellent photocatalytic water splitting, Chem. Eng. J. 468 (2023), 143604.

[20] Z. Li, J. Liu, J. Zhao, R. Shi, G.I.N. Waterhouse, X.D. Wen, T. Zhang, Photo-Driven Hydrogen Production from Methanol and Water using Plasmonic Cu Nanoparticles Derived from Layered Double Hydroxides, Adv. Funct. Mater. 33 (2022) 2213672.

[21] J. Liu, Y. Liu, N. Liu, Y. Han, X. Zhang, H. Huang, Y. Lifshitz, S.T. Lee, J. Zhong, Z. Kang, Metal-free efficient photocatalyst for stable visible water splitting via a two-electron pathway, Science 347 (2015) 970–974.

[22] H. Chang, X. Li, L. Shi, Y.-R. Zhu, T.-F. Yi, Towards high-performance electrocatalysts and photocatalysts: Design and construction of MXenes-based nanocomposites for water splitting, Chem. Eng. J. 421 (2021) 129944.

[23] X. Zhang, C. Xu, L. Zhang, Z. Li, J. Hong, Y. Zhang, Photothermal Catalytic Water Splitting at Diverse Two-Phase Interfaces Based on Cu–TiO$_2$, ACS Appl. Energ. Mater. 5 (2022) 4564–4576.

[24] J. Gao, L. Tang, Z. Shen, Y. Dong, Z. Wang, J. Lyu, J. Li, H. Yu, Efficient solar-light conversion for optimizing the catalytic ozonation of gaseous toluene with PdO$_x$-LaFeO$_3$, Appl. Catal. B-Environ. 288 (2021) 120004.

[25] W.-J. Ong, L.-L. Tan, Y.H. Ng, S.-T. Yong, S.-P. Chai, Graphitic Carbon Nitride (g-C$_3$N$_4$)-Based Photocatalysts for Artificial Photosynthesis and Environmental Remediation: Are We a Step Closer To Achieving Sustainability? Chem. Rev. 116 (2016) 7159–7329.

[26] X. Li, J. Lin, J. Li, H. Zhang, X. Duan, H. Sun, Y. Huang, Y. Fang, S. Wang, Temperature-Induced Variations in Photocatalyst Properties and Photocatalytic Hydrogen Evolution: Differences in UV, Visible, and Infrared Radiation, ACS Sustain. Chem. Eng. 9 (2021) 7277–7285.

[27] H. Ou, L. Lin, Y. Zheng, P. Yang, Y. Fang, X. Wang, Tri-s-triazine-Based Crystalline Carbon Nitride Nanosheets for an Improved Hydrogen Evolution, Adv. Mater. 29 (2017).

[28] L. Yang, J. Liu, L. Yang, M. Zhang, H. Zhu, F. Wang, J. Yin, Co$_3$O$_4$ imbedded g-C$_3$N$_4$ heterojunction photocatalysts for visible-light-driven hydrogen evolution, Renew. Energy 145 (2020) 691–698.

[29] C.Y. Xu, W.H. Huang, Z. Li, B.W. Deng, Y.W. Zhang, M.J. Ni, K.F. Cen, Photothermal Coupling Factor Achieving CO$_2$ Reduction Based on Palladium-Nanoparticle-Loaded TiO$_2$, ACS Catal. 8 (2018) 6582–6593.

[30] M. Ghoussoub, M.K. Xia, P.N. Duchesne, S. Segal, G. Ozin, Principles of photothermal gas-phase heterogeneous CO$_2$ catalysis, Energy Environ. Sci. 12 (2019) 1122–1142.

[31] T. Yagasaki, K. Iwahashi, S. Saito, I. Ohmine, A theoretical study on anomalous temperature dependence of pKw of water, J. Chem. Phys. 122 (2005), 144504.

[32] X. Bian, Y. Zhao, G.I.N. Waterhouse, Y. Miao, C. Zhou, L.Z. Wu, T. Zhang, Quantifying the Contribution of Hot Electrons in Photothermal Catalysis: A Case Study of Ammonia Synthesis over Carbon-supported Ru Catalyst, Angew. Chem. Int. Ed. 62 (2023) e202304452.

[33] Y. Jiang, M. Li, Y. Mi, L. Guo, W. Fang, X. Zeng, T. Zhou, Y. Liu, The influence of piezoelectric effect on the heterogeneous photocatalytic hydrogen production of strontium titanate nanoparticles, Nano Energy 85 (2021), 105949.

[34] Q. Wang, K. Domen, Particulate Photocatalysts for Light-Driven Water Splitting: Mechanisms, Challenges, and Design Strategies, Chem. Rev. 120 (2020) 919–985.

[35] L. Tian, X. Guan, Y. Dong, S. Zong, A. Dai, Z. Zhang, L. Guo, Improved overall water splitting for hydrogen production on aluminium-doped SrTiO$_3$ photocatalyst via tuned surface band bending, Environ. Chem. Lett. 21 (2023) 1257–1264.

[36] X. Yue, S. Yi, R. Wang, Z. Zhang, S. Qiu, Well-controlled SrTiO$_3$@Mo$_2$C core-shell nanofiber photocatalyst: Boosted photo-generated charge carriers transportation and enhanced catalytic performance for water reduction, Nano Energy 47 (2018) 463–473.

[37] S. Patial, V. Hasija, P. Raizada, P. Singh, A.A.P. Khan Singh, A.M. Asiri, Tunable photocatalytic activity of SrTiO$_3$ for water splitting: Strategies and future scenario, J. Environ. Chem. Eng. 8 (2020), 103791.

[38] T. Baran, Efficiency of volatile organic compound degradation in air using doped strontium titanate photocatalysts. Quenching experiments towards understanding of doping mechanisms, React. Kinet. Mech. Catal. 136 (2023) 3243–3256.

[39] Y. Ham, T. Hisatomi, Y. Goto, Y. Moriya, Y. Sakata, A. Yamakata, J. Kubota, K. Domen, Flux-mediated doping of SrTiO$_3$ photocatalysts for efficient overall water splitting, J. Mater. Chem. A 4 (2016) 3027–3033.

[40] Y. Sakata, Y. Miyoshi, T. Maeda, K. Ishikiriyama, Y. Yamazaki, H. Imamura, Y. Ham, T. Hisatomi, J. Kubota, A. Yamakata, K. Domen, Photocatalytic property of

[41] metal ion added SrTiO$_3$ to Overall H$_2$O splitting, Appl. Catal. A-Gen. 521 (2016) 227–232.

[41] Y. Goto, T. Hisatomi, Q. Wang, T. Higashi, K. Ishikiriyama, T. Maeda, Y. Sakata, S. Okunaka, H. Tokudome, M. Katayama, S. Akiyama, H. Nishiyama, Y. Inoue, T. Takewaki, T. Setoyama, T. Minegishi, T. Takata, T. Yamada, K. Domen, A Particulate Photocatalyst Water-Splitting Panel for Large-Scale Solar Hydrogen Generation, Joule 2 (2018) 509–520.

[42] H. Nishiyama, T. Yamada, M. Nakabayashi, Y. Maehara, M. Yamaguchi, Y. Kuromiya, Y. Nagatsuma, H. Tokudome, S. Akiyama, T. Watanabe, R. Narushima, S. Okunaka, N. Shibata, T. Takata, T. Hisatomi, K. Domen, Photocatalytic solar hydrogen production from water on a 100–m2 scale, Nature 598 (2021) 304–307.

[43] J. Tao, J.P. Perdew, V.N. Staroverov, G.E. Scuseria, Climbing the density functional ladder: nonempirical meta-generalized gradient approximation designed for molecules and solids, Phys. Rev. Lett. 91 (2003), 146401.

[44] J.P. Perdew, K. Burke, M. Ernzerhof, Generalized Gradient Approximation Made Simple, Phys. Rev. Lett. 77 (1996) 3865–3868.

[45] S. Grimme, J. Antony, S. Ehrlich, H. Krieg, A consistent and accurate ab initio parametrization of density functional dispersion correction (DFT-D) for the 94 elements H-Pu, J. Chem. Phys. 132 (2010), 154104.

[46] C. Hartwigsen, S. Goedecker, J. Hutter, Relativistic separable dual-space Gaussian pseudopotentials from H to Rn, Phys. Rev. B 58 (1998) 3641–3662.

[47] T. Lu, Q.X. Chen, Shermo: A general code for calculating molecular thermochemistry properties, Comput. Theor. Chem. 1200 (2021).

[48] Y.L. Qin, F. Fang, Z.Z. Xie, H.W. Lin, K. Zhang, X. Yu, K. Chang, La, Al-Codoped SrTiO$_3$ as a Photocatalyst in Overall Water Splitting: Significant Surface Engineering Effects on Defect Engineering, ACS Catal. 11 (2021) 11429–11439.

[49] K. Han, D.M. Haiber, J. Knoppel, C. Lievens, S. Cherevko, P. Crozier, G. Mul, B. Mei, CrO(x)-Mediated Performance Enhancement of Ni/NiO-Mg:SrTiO(3) in Photocatalytic Water Splitting, ACS Catal. 11 (2021) 11049–11058.

[50] F. Fang, F. Xu, Z. Su, X. Li, W. Han, Y. Qin, J. Ye, K. Chang, Understanding targeted modulation mechanism in SrTiO$_3$ using K$^+$ for solar water splitting, Appl. Catal. B-Environ. 316 (2022), 121613.

[51] T. Takata, J. Jiang, Y. Sakata, M. Nakabayashi, N. Shibata, V. Nandal, K. Seki, T. Hisatomi, K. Domen, Photocatalytic water splitting with a quantum efficiency of almost unity, Nature 581 (2020) 411–414.

[52] F.A. Rabuffetti, H.-S. Kim, J.A. Enterkin, Y. Wang, C.H. Lanier, L.D. Marks, K. R. Poeppelmeier, P.C. Stair, Synthesis-Dependent First-Order Raman Scattering in SrTiO$_3$ Nanocubes at Room Temperature, Chem. Mater. 20 (2008) 5628–5635.

[53] K. Maeda, K. Domen, Photocatalytic Water Splitting: Recent Progress and Future Challenges, J. Phys. Chem. Lett. 1 (2010) 2655–2661.

[54] Y.S. Zhu, P.A. Salvador, G.S. Rohrer, Controlling the Relative Areas of Photocathodic and Photoanodic Terraces on the SrTiO$_3$(111) Surface, Chem. Mater. 28 (2016) 5155–5162.

[55] X. Zhang, C. Pei, X. Chang, S. Chen, R. Liu, Z.J. Zhao, R. Mu, J. Gong, FeO$_6$ Octahedral Distortion Activates Lattice Oxygen in Perovskite Ferrite for Methane Partial Oxidation Coupled with CO$_2$ Splitting, J. Am. Chem. Soc. 142 (2020) 11540–11549.

[56] T. Takata, K. Domen, Defect Engineering of Photocatalysts by Doping of Aliovalent Metal Cations for Efficient Water Splitting, J. Phys. Chem. C 113 (2009) 19386–19388.

[57] Z. Su, F. Fang, X. Li, W. Han, X. Liu, K. Chang, Synergistic surface oxygen defect and bulk Ti^{3+} defect engineering on SrTiO$_3$ for enhancing photocatalytic overall water splitting, J. Colloid Interface Sci. 626 (2022) 662–673.

[58] H.J. Jang, S.J. Park, J.H. Yang, S.-M. Hong, C.K. Rhee, D. Kim, Y. Sohn, Photocatalytic and photoelectrocatalytic properties of Eu(III)-doped perovskite SrTiO$_3$ nanoparticles with dopant level approaches, Mater. Sci. Semicond. Process. 132 (2021), 105919.

[59] Y. Li, S. Niu, Y. Hao, W. Zhou, J. Wang, J. Liu, Role of oxygen vacancy on activity of Fe-doped SrTiO$_3$ perovskite bifunctional catalysts for biodiesel production, Renew. Energy 199 (2022) 1258–1271.

[60] J.B. Priebe, M. Karnahl, H. Junge, M. Beller, D. Hollmann, A. Bruckner, Water reduction with visible light: synergy between optical transitions and electron transfer in Au-TiO$_2$ catalysts visualized by in situ EPR spectroscopy, Angew. Chem. Int. Ed. 52 (2013) 11420–11424.

[61] T. Tangcharoen, J. T-Thienprasert, C. Kongmark, Effect of calcination temperature on structural and optical properties of MAl$_2$O$_4$ (M = Ni, Cu, Zn) aluminate spinel nanoparticles, J. Adv. Ceram. 8 (2019) 352-366.

[62] W. Chen, H. Liu, X.Y. Li, S. Liu, L. Gao, L.Q. Mao, Z.Y. Fan, W.F. Shangguan, W. J. Fang, Y.S. Liu, Polymerizable complex synthesis of SrTiO$_3$:(Cr/Ta) photocatalysts to improve photocatalytic water splitting activity under visible light, Appl. Catal. B-Environ. 192 (2016) 145–151.

[63] M. Muralidharan, V. Anbarasu, A. Elaya Perumal, K. Sivakumar, Studies on multifunctional behaviour of Cr doped SrWO$_4$ Compounds, J. Mater. Sci.: Mater. Electron. 26 (2015) 6926–6938.

[64] E. Padmini, K. Ramachandran, Investigation on versatile behaviour of Cd doped SrTiO$_3$ perovskite structured compounds, Solid State Commun. 302 (2019), 113716.

[65] Q. Zhang, Y. Huang, S. Peng, T. Huang, J.-J. Cao, W. Ho, S. Lee, Synthesis of SrFe$_x$Ti$_{1-x}$O$_{3-\delta}$ nanocubes with tunable oxygen vacancies for selective and efficient photocatalytic NO oxidation, Appl. Catal. B-Environ. 239 (2018) 1–9.

[66] Z. Zhao, E.J. Willard, H. Li, Z. Wu, R.H.R. Castro, F.E. Osterloh, Aluminum enhances photochemical charge separation in strontium titanate nanocrystal photocatalysts for overall water splitting, J. Mater. Chem. A 6 (2018) 16170–16176.

[67] Y.F. Zhao, W. Gao, S.W. Li, G.R. Williams, A.H. Mahadi, D. Ma, Solar-versus Thermal-Driven Catalysis for Energy Conversion, Joule 3 (2019) 920–937.

[68] S. Huang, F. Wang, G. Zhang, C. Song, Y. Lei, Q. Xing, C. Wang, Y. Zhang, J. Zhang, Y. Xie, L. Mu, C. Cong, M. Huang, H. Yan, From Anomalous to Normal: Temperature Dependence of the Band Gap in Two-Dimensional Black Phosphorus, Phys. Rev. Lett. 125 (2020), 156802.

[69] Q. Chen, B. Wei, Y. Wei, P. Zhai, W. Liu, X. Gu, Z. Yang, J. Zuo, R. Zhang, Y. Gong, Synergistic effect in ultrafine PtNiP nanowires for highly efficient electrochemical hydrogen evolution in alkaline electrolyte, Appl. Catal. B-Environ. 301 (2022), 120754.

[70] X.J. Li, H.Y. Zhang, Y.Z. Liu, X.G. Duan, X.Y. Xu, S.M. Liu, H.Q. Sun, S.B. Wang, Synergy of NiO quantum dots and temperature on enhanced photocatalytic and thermophoto hydrogen evolution, Chem. Eng. J. 390 (2020), 124634.

[71] Y.C. Du, Y.R. Xue, C. Zhang, Y.X. Liu, Y. Fang, C.Y. Xing, F. He, Y.L. Li, Photoinduced Electrocatalysis on 3D Flexible OsOx Quantum Dots, Adv. Energy Mater. 11 (2021) 2100234.

[72] L. Yin, Y.-P. Yuan, S.-W. Cao, Z. Zhang, C. Xue, Enhanced visible-light-driven photocatalytic hydrogen generation over g-C$_3$N$_4$ through loading the noble metal-free NiS$_2$ cocatalyst, RSC Adv. 4 (2014) 6127–6132.

[73] Z.K. Zhao, Y.T. Dai, J.H. Lin, G.R. Wang, Highly-Ordered Mesoporous Carbon Nitride with Ultrahigh Surface Area and Pore Volume as a Superior Dehydrogenation Catalyst, Chem. Mater. 26 (2014) 3151–3161.

[74] A. Kheradmand, Y.X. Zhu, W.W. Zhang, A. Marianov, Y.J. Jiang, Cobalt oxide on mesoporous carbon nitride for improved photocatalytic hydrogen production under visible light irradiation, Int. J. Hydrog. Energy 44 (2019) 17930–17942.

[75] Z. Li, X. Zhang, L. Zhang, C. Xu, Y. Zhang, Pathway Alteration of Water Splitting via Oxygen Vacancy Formation on Anatase Titanium Dioxide in Photothermal Catalysis, J. Phys. Chem. C 124 (2020) 26214–26221.

[76] K. Maeda, K. Teramura, D. Lu, N. Saito, Y. Inoue, K. Domen, Roles of Rh/Cr$_2$O$_3$ (Core/Shell) Nanoparticles Photodeposited on Visible-Light-Responsive (Ga$_{1-x}$Zn$_x$)(N$_{1-x}$O$_x$) Solid Solutions in Photocatalytic Overall Water Splitting, J. Phys. Chem. C 111 (2007) 7554–7560.

[77] K. Maeda, K. Teramura, D. Lu, N. Saito, Y. Inoue, K. Domen, Noble-metal/Cr$_2$O$_3$ core/shell nanoparticles as a cocatalyst for photocatalytic overall water splitting, Angew. Chem. Int. Ed. 45 (2006) 7806–7809.

[78] F. Zhang, A. Yamakata, K. Maeda, Y. Moriya, T. Takata, J. Kubota, K. Teshima, S. Oishi, K. Domen, Cobalt-Modified Porous Single-Crystalline LaTiO$_2$N for Highly Efficient Water Oxidation under Visible Light, J. Am. Chem. Soc. 134 (2012) 8348–8351.

[79] L. Zhang, X. Zhang, H. Mo, J. Hong, S. Yang, Z. Zhan, C. Xu, Y. Zhang, Synergistic Modulation between Non-thermal and Thermal Effects in Photothermal Catalysis based on Modified In$_2$O$_3$, ACS Appl. Mater. Interfaces 15 (2023) 39304–39318.